The Role of Connectivity in Thermal Imaging

AHMED AMIN

Naval Sea Systems Command, Division Newport, Newport, RI 02841, USA

Abstract. This paper demonstrates the role of connectivity, a concept originally developed by Newnham two decades ago, in improving image quality of infrared (IR) imaging systems by enhancing the thermal modulation transfer function (MTF). IR imaging in the medium wavelength range (7.5 to 14 μm), corresponding to the thermal black body maximum near room temperature and to the atmospheric window, is desirable for a wide range of applications. Night vision, target recognition, reconnaissance, driving aids, and navigation in foggy and poor visibility weather are among the applications of this technology. 1:3 arrays fabricated from ceramic barium strontium titanate (BST) have made it possible to produce compact, low-cost, uncooled infrared cameras that are capable of delivering television quality images.

Keywords: infrared imaging, dielectric bolometer, thermal imaging

1. Introduction

The pioneering work of Newnham and colleagues on composites, phase assembly, connectivity, macro-symmetry, property optimization, and smart materials is well recognized; see for example references [1–7]. Three basic *design rules* have evolved to aid in fabricating effective composites. These are *connectivity, symmetry, and scale. Connectivity* is the mode of self interconnection of the phases. It controls the fluxes and fields in the system, thereby enabling property tensor tailoring. *Symmetry* of the individual phases and the macro-symmetry of their assemblage in the composite can be used for additional control. *Scale* of the composite phases controls the mode averaging for the property coefficients. Resonance can occur when the wavelength λ of the excitation is comparable to the scale of the composite.

One class of problems where the connectivity design rules were successfully applied is thermal budget optimization in uncooled focal plane (UFP) barium strontium titanate (BST) pyroelectric imaging detectors. Lateral thermal diffusion in the BST detectors has a significant effect on signal degradation. Detector reticulation to produce a 1:3 connectivity pattern (arrays) enhances the thermal modulation transfer function (MTF)

as will be discussed in detail in Section 5. This quantity is related to signal losses as a result of thermal spreading caused by in-plane thermal diffusion.

Thermal detectors are generally based on two different modes of operation. The two technologies considered most seriously are thermistor bolometers and pyroelectric detectors. Both technologies offer the capability to operate near room temperature without the need for extensive cooling. A thermistor bolometer is a sensitive means to detect thermal effect of infrared radiation [8, 9]. In this technology, the rapid change of resistance with temperature of semiconductors negative temperature coefficient (NTC) and positive temperature coefficient (PTC) thermistors is utilized.

The basic problem of processing thermal images stems from low-level signals of interest. They represent a small component of the total detectable radiation flux. In addition, dark current level (in the absence of incident flux) further limits the sensitivity of thermal detectors. This effect is relatively inconsequential for point detectors. For scanned linear arrays this problem has been solved by ac coupling the output of each pixel. This is not an acceptable solution for densely populated two-dimensional staring arrays for two reasons: (1) the limited real estate on the readout circuitry, and (2) the low operating frequency requires large ac coupling

capacitors. Pyroelectric detectors, on the other hand, are ac-coupled devices, thereby reducing system complexities by providing a practical solution to the problems of detecting small signals in a fairly large background thermal scene. A hybrid approach with thermally isolated detector array, solder bump-bonded, pixel by pixel to the silicon readout circuitry (ROC) was pioneered independently by Texas Instruments [10, 11], Honeywell [12], and Plessey [13]. In this article we will briefly describe pyroelectric operation modes, pyroelectric thermal detection and figures of merit, noise sources and sensitivity limits, connectivity, signal enhancement and spatial resolution, imaging array and system description.

2. Pyroelectric Operation Modes

The short circuit (current mode) pyroelectric coefficient p is defined as

$$p = (\partial P/\partial T)_E. \qquad (1)$$

In the MKS system of units, the polarization vector P (i.e., the charge per unit area taken perpendicular to P) has the units Cm^{-2}. Therefore, the pyroelectric coefficient is expressed as $Cm^{-2}\,K^{-1}$, or more often in the literature as $\mu Ccm^{-2}\,K^{-1}$. If a pyroelectric crystal with a metallized surface area A (perpendicular to the polar axis) is subjected to a uniform heating rate $(\partial T/\partial t)$, the pyroelectric current is expressed as

$$I = pA(\partial T/\partial t). \qquad (2)$$

The open circuit (voltage mode) pyroelectric coefficient $(Vm^{-1}\,K^{-1})$ is given by the following identity,

$$(\partial E/\partial T)_P = (\partial P/\partial T)_E(\partial E/\partial P)_T = p/\varepsilon, \qquad (3)$$

where ε is the dielectric permittivity (Fm^{-1}). Noting that $P = \varepsilon_0\chi E$ where χ is the dielectric susceptibility, we get $(\partial P/\partial E)_T = \varepsilon_0\chi$. The relative permittivity (dielectric constant) is given by $\varepsilon_r = \varepsilon/\varepsilon_0 = (1 + \chi)$, therefore, we may write for high dielectric constant materials, $\varepsilon = \varepsilon_0\chi$ and $(\partial E/\partial P)_T = 1/\varepsilon$.

Let's consider electric field biased E_b operation of a pyroelectric-ferroelectric material with a spontaneous polarization P_s. There are significant performance gains from this mode of operation, which will

become evident from the analysis that follows. The dielectric displacement D takes the form,

$$D = \varepsilon E_b + P_s$$
$$(\partial D/\partial T)_E = p' = (\partial\varepsilon/\partial T)_E E_b + (\partial P_s/\partial T)_E, \qquad (4)$$

where p' is the total pyroelectric coefficient. The first term on the right hand side in the equation above is the dielectric contribution (bolometer mode), whereas the second term is the spontaneous polarization contribution (pyroelectric mode). Rigorously, the dielectric contribution term should be written as a field integral to account for dielectric nonlinearities of the ferroelectric material. We also have,

$$(\partial E/\partial T)_D = (\partial D/\partial T)_E/(\partial D/\partial E)_T = p'/\varepsilon$$
$$= (1/\varepsilon)[(\partial\varepsilon/\partial T)_E E_b + (\partial P_s/\partial T)_E] \qquad (5)$$

We must emphasize that p' and $(\partial E/\partial T)_D$ do not vary linearly with bias field E_b as implied by the equations above. This is because of the nonlinear dielectric response to E_b. The derived quantities p' and p'/ε, are related to the material figures of merit as will be described next. The principle of detector operation near the transition temperature T_t, where properties are maxima, is schematically illustrated in Fig. 1. A dc bias field is applied to prevent depoling and boost signal. Properties of some pyroelectric-ferroelectric barium strontium titanate BST compositions [14] are listed in Table 1.

We conclude this section by emphasizing that pyroelectricity is a null property in many crystal systems.
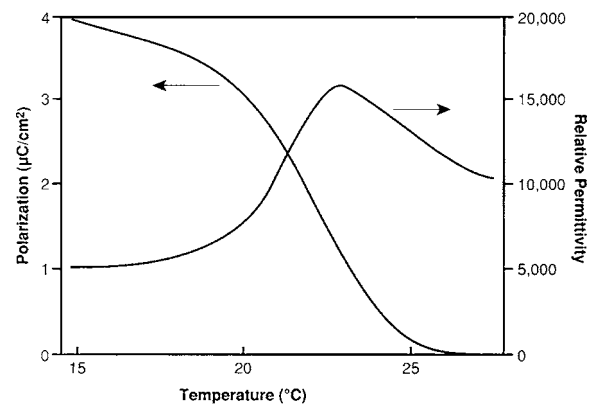

Fig. 1. A schematic depiction of the polarization and dielectric responses of a ferroelectric bolometer.

Table 1. Properties of DC-biased barium strontium titanate BST [14].

Ba/Sr ratio	Bias (kV/cm)	T_t (C)	p'_{max} (μCcm^{-2} K^{-1})	ε	$\tan\delta$	F_J (cm^3 J^{-1})$^{1/2}$	F_v (cm^2 C^{-1})
67/33	1	21	23	31000	0.028	0.84	2700
67/33	2	22	6.3	33000	0.021	0.25	670
67/33	6	24	0.70	8800	0.004	0.12	280

$F_v = p'/c_p \varepsilon_0 \varepsilon$.
$F_J = p'/c_p (\varepsilon \varepsilon_0 \tan\delta)^{1/2}$.
$c_p = 3.2$ (Jcm^{-3} K^{-1}).

There are certain requirements imposed by the crystal symmetry group for pyroelectricity to occur: (1) the absence of an inversion operation and (2) the existence of a unique polar axis. Therefore, pyroelectricity is limited to the following 10 crystallographic point groups: $1(C_1)$, $2(C_2)$, $3(C_3)$, $4(C_4)$, $6(C_6)$, m (C_s), mm2 (C_{2v}), 3 m(C_{3v}), 4 mm(C_{4v}), 6 mm(C_{6v}), in addition to the limiting group ∞mm$(C_{\infty v})$ which represents that of an electrically poled ferroelectric ceramic. The direction of the pyroelectric vector is along the unique polar axis, i.e., 2, 3, 4, 6, or ∞ in the preceding groups. It is arbitrarily set for point group $1(C_1)$ and lies in the mirror plane for m (C_s).

We have presented the material properties (scalar form) that are necessary for analyzing the performance (signal and noise) of a pyroelectric bolometer. Rigorously, the tensor representation should be used for completeness and deeper insights. In a polarizable deformable nonlinear dielectric such as bonded ferroelectric BST arrays, the effect of elastic, thermal, and electrical boundaries on the pyroelectric signal must be underscored [15]. For instance, the pyroelectric effect in a mechanically "free" and "clamped" crystal could differ greatly (both in magnitude and sign). Nonuniform heating causes undesirable signal due to tertiary pyroelectricity. On the other hand, the effect of bias field on the pyroelectric signal is influenced by the order of ferroelectric phase transition.

3. Pyroelectric Thermal Detection and Figures of Merit

The pyroelectric detector equivalent circuit can be represented by a current source $I = Ap(dT/dt)$ driving a parallel detector-load impedance. If C_d and R_d are the capacitance and leakage resistance of the detector and R_L and C_L are load resistance and capacitance (deliberate or parasitic), thus, the parallel detector-load capacitance C_E and resistance R_E are: $C_E = (C_d + C_L)$ and $R_E^{-1} = G_E = R_d^{-1} + R_L^{-1}$. Where G_E, is the electrical conductance and $C_d = \varepsilon_0 \varepsilon A/z$ with z being the detector thickness. The circuit admittance is $Y = G_E + i\omega C_E$.

The detector (BST pixel) shown in Fig. 2 is represented by a thermal capacitance H connected by a thermal conductance G_T to the surrounding (mesa, readout silicon IC, etc.). Solution of the heat transfer equation for a sinusoidally modulated incident thermal power $W = We^{i\omega t}$, yields the following expression for the detector voltage responsivity R_v

$$R_v = |I/YW|$$
$$= \eta\omega pA/[G_T G_E (1 + \omega^2\tau_T^2)^{1/2}(1 + \omega^2\tau_E^2)^{1/2}], \tag{6}$$

where η is the fraction of incident power absorbed by the detector, A is the detector area, $\tau_T (= H/G_T)$ and $\tau_E (= C_E/G_E)$ are the thermal and electrical time constants, respectively. The voltage responsivity R_v has the following characteristics:

1. A maximum at a frequency $f = 1/2\pi(\tau_T\tau_E)^{1/2}$, given by R_v (max) $= \eta pA/G_T G_E(\tau_T + \tau_E)$,
2. A flat response within 3 dB of R_v (max), in the region bounded by the thermal and electrical relaxation frequencies,
3. For frequencies higher than the characteristic frequency $f (= 1/2\pi\tau_E)$, the response is attenuated by C_L, i.e., $R_v = \eta p/z\omega c_p(C_d + C_L)$, where c_p is the heat capacity per unit volume. Nonetheless, R_v exhibits a $1/f$ behavior.

Detector material figures of merit can be readily defined from the responsivity equation. For instance, if $C_d \gg C_L$ then $R_v = \eta p/Ac_p\varepsilon$, and a voltage responsivity figure of merit F_v may be taken as $p/c_p\varepsilon_0\varepsilon$. On the other hand if $C_d \ll C_L$, a current responsivity figure

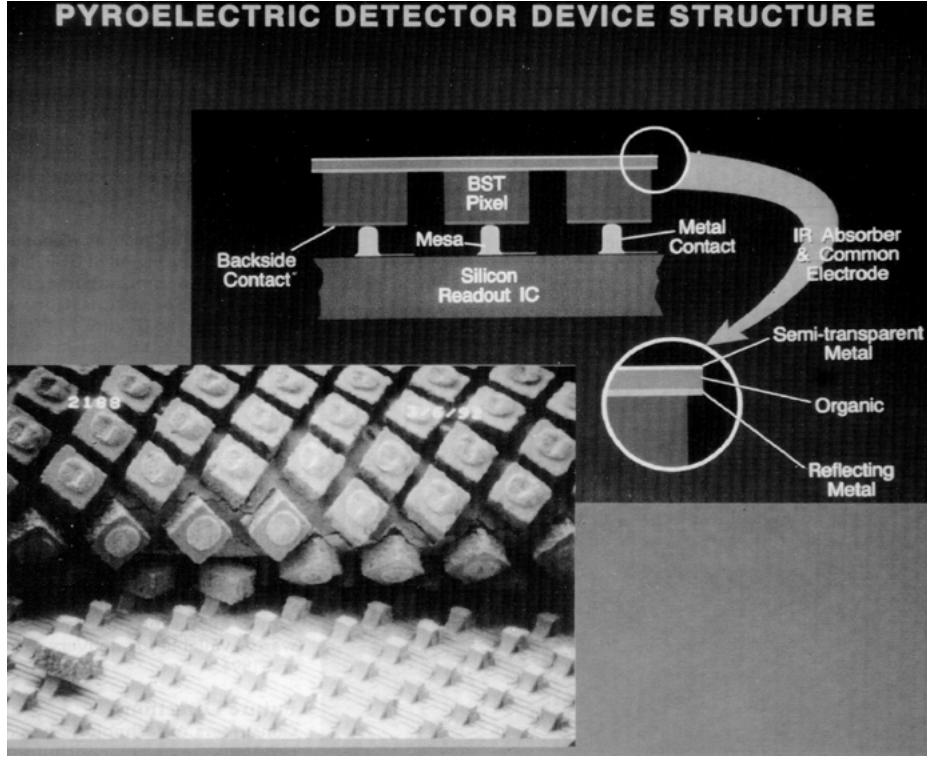**PYROELECTRIC DETECTOR DEVICE STRUCTURE**

Fig. 2. Array structure (a peel off) showing the BST pixels, and the mesa for thermal isolation. The inset depicts vertical integration (hybrid process) of optical coating, BST, interconnect, and polymer mesa on the Si substrate [11]. Note: The 1:3 connectivity pattern of BST pixels. According to this notation, the BST elements are connected in one dimension, e.g., along the z-axis in the elevation plane and totally disconnected in the target, i.e., xy-plane (Fig. 2). The second phase (xenon or air) surrounding the pixels is three dimensionally connected.

of merit F_i may be taken as p/c_p. An additional figure of merit F_J, related to noise limited sensitivity will be introduced in the next section.

4. Noise Sources and Sensitivity Limits

The pyroelectric detector sensitivity is limited by three noise sources; namely, Johnson, temperature fluctuation, and amplifier current and voltage. Johnson noise is also known as the dielectric loss noise. There are two sources by which Johnson noise is generated in a capacitive detector (1) leakage and (2) poor electrical contacts. A leaky capacitor is represented by an ideal capacitance C_d in parallel with a resistance R_d. The impedance Z_p is $Z_p = R_d/(1 + i\omega R_d C_d)$, where $R_d = 1/(\omega C_d \tan \delta)$. For a high quality ferroelectric, $\tan \delta$ is very small (<0.01), hence dielectric loss contribution is insignificant. Poor electrical contacts can have a profound effect on losses. A series resistance

R_s can contribute to dielectric losses. The impedance of a series capacitance–resistance circuit is $Z_s = R_s + (1/i\omega C_d)$, where $\tan \delta = \omega R_s C_d$. The series resistance has to be in the $\sim 10^6 \, \Omega$ range to significantly contribute to losses. The spectral density of Johnson noise is $v_J^2 = 4kT[R_E/(1 + \omega^2 R_E^2 C^2)]$, where $R_E = R_d R_L/(R_d + R_L)$ is the total parallel detector–load resistance, and $C_E = C_d + C_L$ is the total parallel detector–load capacitance. For high frequency or large R_L we have

$$v_J^2 = 4kT(\tan \delta/\omega)\big[C_d/\big(C_E^2 + C_d^2 \tan^2 \delta\big)\big] \quad \text{or}$$
$$\sim 4kT(\tan \delta/\omega)[C_d/(C_d + C_L)^2]$$

for low loss ferroelectrics.

From the expression above, the dielectric loss noise has the following characteristics, (1) it is attenuated by the load capacitance C_L; (2) it behaves as $1/f$ noise at higher frequencies; (3) at lower frequencies R_L dominates the impedance and the response is flat. From the definition of detector sensitivity $D^* = (R_v/v_J)$, a figure

of merit F_J for detectors limited by Johnson noise is taken as $F_J = p/c_p(\varepsilon\varepsilon_0 \tan \delta)^{1/2}$.

Temperature fluctuation noise is the limiting factor of the sensitivity of thermal detectors. It is the signature of the random exchange heat transfer by photons (radiation), phonon (conduction) or convection between the detector and its surroundings. The voltage fluctuation spectrum for a bandlimited detector is

$$v_T^2 = (4kT/H)[pA/(C_d + C_L)]^2\big[\tau_T/\big(1 + \omega^2\tau_T^2\big)\big]$$
$$\times \big[\omega^2\tau_E^2/\big(1 + \omega^2\tau_E^2\big)\big]. \quad (7)$$

If the characteristic frequency $f_E(= 1/2\pi\tau_E)$ of the high-pass filter is comparable with the thermal bandwidth, then the noise is significantly suppressed. Otherwise, if τ_E is large, then the high pass filter has very little effect on the noise. As it turns out $D_T^* = (R_v/v_T) = \eta(A/4kT^2 G_T)^{1/2}$ is independent of material parameters.

5. Connectivity, Signal Enhancement, and Spatial Resolution

Connectivity is a key feature in property development in multiphase solids. Physical properties can change many orders of magnitude depending upon the manner in which connections are made. Each phase in a composite may be self connected in zero, one, two, and three dimensions. In three dimensions, there are ten connectivities for diphasic composites [1]: 0-0, 1-0, 2-0, 3-0, 1-1, 2-1, 3-1, 2-2, 2-3, and 3-3. A 2-1 connectivity pattern, for example, has one phase self connected in two dimensional chains or fibers. The connectivity patterns are not generally unique. In the case of a 2-1 pattern, the fibers of the second phase might be perpendicular to the layers of the first phase or they might be parallel to the layers. For n phases the number of connectivity patterns is $(n+3)!/3!n!$. There are 20 three-phase patterns and 35 four-phase patterns. Three-phase patterns are important when electrode patterns are incorporated in the diphasic ceramic structures [3].

Dielectric bolometers fabricated from polycrystalline BST are characterized by high electrical resistivity, therefore, no signal degradation will occur as a result of charge spreading. On the other hand, they suffer from a large lateral thermal diffusion coefficient D_T. As a result, the thermal distribution in the target (detector) plane will be degraded, and so will the signal

levels. The spatial resolution on the target plane is determined in accordance with the thermal modulation transfer function MTF,

$$\text{MTF} = (f_c/\pi^2 D_T n^2)\tan\text{h}(\pi^2 D_T n^2/f_c), \quad (8)$$

where D_T is the lateral thermal diffusion coefficient $(\text{m}^2\text{s}^{-1})$, f_c is the chopper frequency (Hz), and n is the spatial frequency (line pair/cm). Note, D_T is defined as the ratio of thermal conductivity κ and the heat capacity per unit volume, $D_T = \kappa/\rho C_p$, where ρ is the density and C_p is the specific heat. Therefore, the voltage responsivity R_v as defined by Eq. (6) is modified according to,

$$R_v(n) = [\text{MTF}][R_v(0)]. \quad (9)$$

The lateral thermal diffusion coefficient for polycrystalline barium titanate BaTiO$_3$ is $\sim 2 \times 10^{-7}$ m^{2}s^{-1}. This is two orders of magnitude larger than that of polymer PVF2 ($\sim 2 \times 10^{-9}$). To compare the MTF for BaTiO$_3$ and PVF$_2$, let's consider a spatial line frequency $n = 80$ line pair/cm (corresponding for instance to 50 μm thermal line width on 75 μm centers), and let the chopper frequency f_c be 50 Hz. The MTF values for polycrystalline BaTiO$_3$ and polymer PVF$_2$ will be 0.39 and 0.99 respectively. To minimize thermal spreading, the BST detector is reticulated (sliced) to form a 1:3 connectivity pattern (pixels). According to this notation, the BST elements are connected in one dimension, e.g., along the z-axis in the elevation plane and totally disconnected in the target, i.e., xy-plane (Fig. 2). The second phase (xenon or vacuum) which surrounds the detector, is three dimensionally connected.

6. Imaging Array Fabrication and System Description

The uncooled focal plane array (UFPA) is fabricated from stoichiometric, doped, compacted, and sintered BST wafers to optimize microstructure and electrical properties. The wafers are ground and polished. After laser reticulation, the wafers are etched to remove the slag, and subsequently annealed in oxygen to reoxidize the surface. The reticulated BST pixels are directly bump bonded to the silicon readout IC. The pixels are on 48.5 μm centers and the kerf is about 10 μm. Reticulation of the BST detector material to produce a 1:3 connectivity array enhances the thermal modulation

transfer function (MTF) as described in the previous section. A resonant cavity IR absorber is formed on the IR sensitive side of the detector. It provided better than 90% average absorption over the 7.5 to 14 μm spectral region. The finished detector is an array of 245 $\times$ 328 pixels with a tight property distribution. Pixel-to-pixel uniformity is an important requirement for an imaging array. Variations in properties from pixel-to-pixel will result in an undesirable fixed pattern noise.

The readout IC is a CMOS device. The unit cell consists of CMOS inverter preamplifier, a highpass filter, a gain stage, a tunable low-pass filter, a buffer and an address switch. The high-pass filter has a characteristic frequency $f_{3db} \sim 10$ Hz. It consists of the pixel capacitance and a large feedback resistor ($\sim 10^{12}$ Ω). The low-pass resistance is a diode whose effective impedance is controlled by an in cell current source. An off chip voltage source determines the current level and the resistance. Therefore, the filter is tunable. The operation of the system is briefly discussed with the aid of the block diagram in Fig. 3. An antireflection Ge window covers the package and allows IR transmission in the 7.5 to 14 μm spectral region. The IR lens (typically $f/1.0$) with 100 mm focal lens projects the IR image on
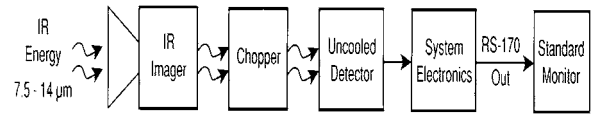
Fig. 3. A block diagram of the thermal imaging system [11].

the focal plane BST array. The array is mounted on a thermoelectric cooler for optimum operation near the ferroelectricparaelectric transition temperature T_c. The chopper provides the thermal modulation (30 Hz/line). The ROIC filters, amplifies, samples, and multiplexes the detector signal one row at a time and delivers the output at a standard RS170 rate.

A useful system performance figure of merit is the noise equivalent temperature difference, NETD. This is the temperature difference at the scene, ΔT_{scene}, that is required to generate an rms signal to noise ratio of 1. A remarkable NETD less than 0.02 K has been achieved with recent pyroelectric imaging cameras fabricated from hybrid BST detectors which operate near room temperature. An example of a still pyroelectric image produced by a BST focal plane array and $f/1.0$ optics is shown in Fig. 4.

Fig. 4. Thermal image produced by the pyroelectric effect in ferroelectrics. The image was taken by a BST detector with NETD $= 0.2$ K and $f/1.0$ optics [14]. Recent detectors NETD $= 0.02$ K.

7. Summary

Impressive progress in thermal imaging using the pyro-electric effect in ferroelectric materials has occurred. It is possible to produce compact, low-cost infrared cameras which operate near room temperature that are capable of delivering television quality images. Detector (BST) reticulation to produce 1:3 array enhances the thermal modulation transfer function (MTF), thereby reducing signal attenuation due to in-plane thermal diffusion. Applications of this technology are varied and include night vision, target recognition, driving and navigation aids in foggy and poor visibility weather, and locating victims in heavy smoke-fire fighting.

Acknowledgment

References

1. R.E. Newnham, D.P. Skinner, and L.E. Cross, *Mat. Res. Bull.*, **13**, 525 (1978).
2. R.E. Newnham, *Annual Rev. Mater. Sci.*, **16**, 47 (1986).
3. R.E. Newnham, *J. Materials Education*, **7**, 60 (1985).
4. R.E. Newnham, *National Institute of Standards and Technology Special Publication 803; Proc. International Conference Chemistry of Ceramic Materials*, **39** (1991).
5. R.E. Newnham and A. Amin, *Chemtech.*, **29**(12), 39 (1999).
6. R.E. Newnham, *Mat. Res. Soc. Bull.*, **22**, 20 (1997).
7. R.E. Newnham, *Bull. Am. Ceram. Soc.*, **75**(10), 51 (1996).
8. G.B. Brandao, L.A.L. de Almeida, G.S. Deep, A.M.N. Lima, and H. Neff, *J. Appl. Phys.*, **90**(4), 1999 (2001).
9. R.J. Keys, *Topics In Applied Physics: Optical and Infrared Detectors* (Springer-Verlag, New York, 1980).

10. G.S. Hopper, U.S. Patent 4,080,532 (1978); **4**, 162402 (1979).
11. *Texas Instruments Technical Journal*, **11**(5), 1 (1994).
12. S. Iwasa, N. Butler, and J. McClelland, *Proc. SPIE*, **151**, 930 (1988).
13. E. H. Putley, *Infrared Phys.*, **20**, 49 (1980).
14. B.M. Kulwicki, A. Amin, H.R. Beratan, and C.M. Hanson, *Proc. IEEE Inter. Sympos. Appl. Ferroelectr.*, 1 (1992).
15. A. Amin, *Texas Instruments Tech. Rep.* (1991).
16. H. Lipson and W. Cochran, *The Determination Of Crystal Structures* (Cornell University Press, Ithaca, New York, 1965).
17. M.J. Buerger, *Crystal Structure Analysis* (John Wiley, New York, 1960).
18. M.J. Buerger, *Vector Space* (John Wiley, New York, 1959).
19. B.E. Warren, *X-Ray Diffraction* (Addison-Wesley, Reading, Mass., 1969 and Dover Publications, New York, 1990).
20. J.F. Nye, *Physical Properties of Crystals, Their Representation By Tensors and Matrices* (Oxford University Press, 1969).
21. W.P. Mason, *Crystal Physics Of Interaction Processes* (Academic Press, New York, 1966).
22. S. Bhagvantam, *Crystal Symmetry and Physical Properties* (Academic Press, New York, 1966).
23. Y.I. Sirotin and M.P. Shaskolskaya, *Fundamentals Of Crystal Physics* (English Translation, Mir Publications, Moscow, 1982).
24. R.R. Birss, *Symmetry and Magnetism* (John Wiley, New York, 1964).
25. A. Amin, R.E. Newnham, and D. Schlom, *Crystal Anisotropy— Lecture Notes* (The Pennsylvania State University, State College, PA, 1999).
26. A.R. Von Hippel, *Dielectrics and Waves* (MIT Press, Cambridge, Mass., 1954).
27. A.R. Von Hippel (Ed.), *Dielectric Materials and Application* (MIT Press, Cambridge, Mass., 1954).
28. R.C. Evans, *An Introduction To Crystal Chemistry* (Cambridge University Press, Canbridge, 1966).
29. L. Pauling, *The Nature Of The Chemical Bond* (Cornell University Press, Ithaca, New York, 1960).
30. R.E. Newnham, *Structure-Property Relations* (Springer-Verlag, New York, 1975).